IST 2009 - International Workshop on Imaging Systems and Techniques
Shenzhen, China
May 11-12, 2009

Iterative and Single-step Solutions of Multi-offset Ultra Wide Band Data in the Time Domain

S. Binajjaj[1], T. Zanoon[1], and M.Z. Abdullah[1]
[1]School of Electrical and Electronic Engineering
Universiti Sains Malaysia
Engineering Campus, Penang 14300 , Malaysia
Tel: (604)-5996001; Fax (604)-5941023; Email: mza@eng.usm.my

Abstract— **This paper deals with the inverse scattering of ultra wide band (UWB) tomography used in reconstruction the dialectic properties of the unknown targets in 2D. The image reconstruction algorithm is based on the gradient minimization of an augmented cost function defined as the different between measured and calculated fields. The computation requires two successive steps: (i) direct and (ii) adjoint solutions. The forward-backward time stepping algorithm, implementing the finite-difference time-domain (FDTD) method with Mur's absorbing boundaries is employed in both steps. The imaging algorithm is based on non-linear optimization technique from which the single-step and iterative inversion schemes are derived. The experimental results demonstrate that the algorithms can resolve features whose sizes are comparable to the half wave-length even though scaterring data are collected only from limited view angles. These experimental evidence suggest that the technique could potentially be used to solve practical imaging problems such as detecting cancerous tumors in breast.**

Keywords: Electromagnetic tomography, ultrawide band, FDTD, inverse problem.

I. INTRODUCTION

Inverse scattering deals with the reconstruction of the electromagnetic properties of a scatterer under investigation, and have attracted the attention of many researchers because of its potential applications in variety of fields such as medical imaging, geophysical exploration, nondestructive testing, and target identifications. A key promising application is breast cancer detection, where thermal and ionizing radiations of CT and MRI are avoided. In addition, the contrast in permittivity properties between malignant and background fat tissue [1] can easily distinguish cancer tumors. Many nonlinear inversion techniques have been proposed for imaging high-contrast objects. The vast majority of these proposed techniques have been based on the frequency domain approach where the incidences are assumed to be monochromatic. Popular frequency-domain methods include the method of moments (MoM) [2, 3] and the finite-element method (FEM)[4].When the frequency of excitation is increased, in order to improve the resolution of the reconstructed scatterer profile, the inversion becomes highly non-linear because of the wave scattering and other soft field related artifacts. On the other hand the high frequency and broad-band signal is a preferred choice for excitation since this signal enables images to be reconstructed at super-resolution accuracy [5-7]. One popular approach to obtain more detailed reconstruction is through the use of time domain methods. One such method is the FDTD which has been successfully investigated for different applications [7, 8].

Recently, the time domain inverse scattering technique based on non-linear optimization methods have been proposed[8, 9]. In this technique, the cost function is represented by the difference between simulated and observed data, and the solution is obtained through iterative minimization. Different minimization techniques are available ranging from local minimization, where first and second order derivatives methods are used, to global minimization, where one attempts to find the global minimum using stochastic methods. Global techniques require large number of cost function evaluations, and hence, are considered more costly than local methods. However, the second order methods utilizing Hessian matrix are too expensive compared to the first order one where only the gradient information has been utilized. Hence, among both optimization classes, the preferred choice in terms of computational cost is the first order method. Popular examples include the steepest descent, the quasi-Newton, and the linear and non-linear conjugate gradient techniques.

The concept of sensitivity analysis design implementing Landweber regularization strategy was introduced for applications in process tomography[10]. Following this the FDTD approach of the inverse-scattering problem using sensitivity map solution was recently proposed in [11] and [12].One particular shortcomings of this inversion strategy is that the sensitivity calculations are computationally intensive, and are not yet efficient enough for large tomographic problems. Furthermore, the quality of the image depends strongly on the threshold values used to map the scattered field vector to the permittivity space, and subsequently, updating this parameter in response to a convergence or divergence. Moreover, the sensitivity kernels are computed using first peak arrival times which are difficult to measure due to scattering and waveform distortion. Clearly, a more realistic model focusing on the information in the full waveform is needed in order to improve the accuracy of the inversion scheme.

In this paper we employ the former approach in calculating the sensitivity or gradient of the scattered fields with respect to the model parameter by using Fréchet derivatives and adjoint-state method [9] and [13]. By utilizing this analytical form of the sensitivity functions, both single step and iterative solutions are attempted. In the first case the algorithm is terminated after the first iteration and the solution is obtained through Born series approximation. Meanwhile, the iterative solution is obtained by repeatedly updating and minimizing the gradient function leading to Newmann series approximation. In the later case the Polak–Ribiére nonlinear conjugate gradient method[14] is used in the minimization. Some salient features of these inversion techniques, particularly the capability of reconstructing an object at super-resolution accuracy, are demonstrated using simulated and real data experiments.

978-1-4244-3483-1/09/$25.00 ©2009 IEEE

II. TIME DOMAIN INVERSE SCATTERING

A. Problem Formulation

We consider a bounded 2-D domain which is occupied by single or multiple scatterers as shown in Fig. 1. These scatterers can only be dielectric and are described by spatial distribution of their dielectric properties. For simplicity, we assume that the medium is non-dispersive and isotropic. The cross-hole geometry is used in the measurement, and the images are reconstructed from limited-view projections.

B. Augmented Cost Function

Following similar procedures described by [9] and [13], and assuming TM mode propagation in which the electric field is polarized in *z* direction, the unknown properties representing the dielectric properties $\varepsilon(x,y)$ can be estimated by minimizing the cost function as follows

$$F\left(\varepsilon,\vec{E}_z\right)=\frac{1}{2}\sum_{n=1}^{N}\sum_{m=1}^{M}\int_0^T\left\|\vec{E}_z^{\,n,m}-\vec{E}_z^{\,'n,m}\right\|^2 dt \qquad (1)$$

where ε is the dielectric property of the scatterers, $\vec{E}_z^{\,n,m}$ and $\vec{E}_z^{\,'n,m}$ respectively represent the measured and calculated fields obtained at the *m*th measurement position for *n*th incident wave.

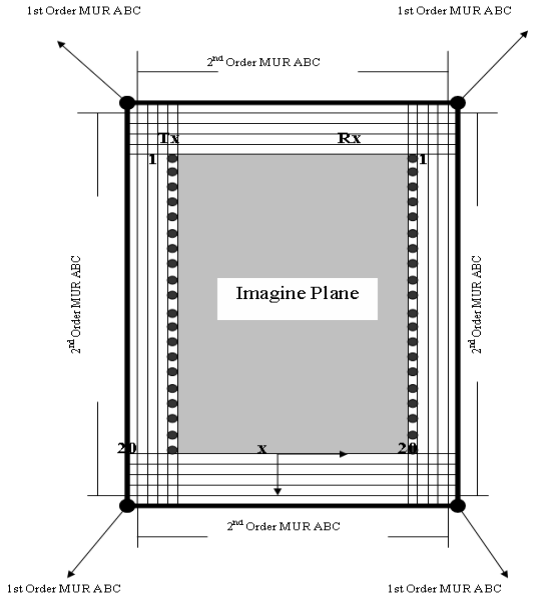

Fig. 1 FDTD grid used to model the propagation of TM's wave in a cross-hole geometry. The grid is truncated by first and second order Mur absorbing boundary conditions [15]

This minimization process is subjected to the constraint in such a way that for given estimate of ε and for every incidence the calculated fields should satisfy the Maxwell's equations. Next, the constraint is introduced to the cost function by utilizing Lagrange multipliers referred to as the adjoint fields and denoted by, $\vec{e}_z^{\,n}$, $\vec{h}_x^{\,n}$ and $\vec{h}_y^{\,n}$. Thus, the objective is to minimize the following augmented cost function

$$F^a(\varepsilon,\vec{E}_z\vec{e}_z^{\,n})=F(\varepsilon,\vec{E}_z)+\sum_{n=1}^{N}\int_0^T\int_\Gamma[\vec{h}_x^{\,n}\ \ \vec{h}_y^{\,n}]\begin{bmatrix}\mu\dfrac{\partial\vec{H}_x^{\,n}}{\partial t}+\dfrac{\partial\vec{E}_z^{\,n}}{\partial y}\\ \mu\dfrac{\partial\vec{H}_y^{\,n}}{\partial t}+\dfrac{\partial\vec{E}_z^{\,n}}{\partial x}\end{bmatrix}d\Gamma dt + \sum_{n=1}^{N}\int_0^T\int_\Gamma\vec{e}_z^{\,n}\left(\frac{\partial\vec{H}_y^{\,n}}{\partial x}-\frac{\partial\vec{H}_x^{\,n}}{\partial y}-\varepsilon\frac{\partial\vec{E}_z^{\,n}}{\partial t}-\sigma\vec{E}_z^{\,n}\right)d\Gamma dt \qquad (2)$$

The necessary condition for the minimization of the augmented cost function is that its first variation is equal to zero. Taking into account only the first-order variations while neglecting all higher order terms, and assuming that the perturbations in parameters μ and σ are zeroes, the first variation can be written as

$$\delta F^a=\sum_{n=1}^{N}\int_0^T\int_\Gamma[\delta\vec{h}_x^{\,n}\ \ \delta\vec{h}_y^{\,n}]\begin{bmatrix}\mu\dfrac{\partial\vec{H}_x^{\,n}}{\partial t}+\dfrac{\partial\vec{E}_z^{\,n}}{\partial y}\\ \mu\dfrac{\partial\vec{H}_y^{\,n}}{\partial t}+\dfrac{\partial\vec{E}_z^{\,n}}{\partial x}\end{bmatrix}d\Gamma dt + \sum_{n=1}^{N}\int_0^T\int_\Gamma\delta\vec{e}_z^{\,n}\left(\frac{\partial\vec{H}_y^{\,n}}{\partial x}-\frac{\partial\vec{H}_x^{\,n}}{\partial y}-\varepsilon\frac{\partial\vec{E}_z^{\,n}}{\partial t}-\sigma\vec{E}_z^{\,n}\right)d\Gamma dt + \delta F+\sum_{n=1}^{N}\int_0^T\int_\Gamma[\vec{h}_x^{\,n}\ \ \vec{h}_y^{\,n}]\begin{bmatrix}\mu\dfrac{\partial\delta\vec{H}_x^{\,n}}{\partial t}+\dfrac{\partial\delta\vec{E}_z^{\,n}}{\partial y}\\ \mu\dfrac{\partial\delta\vec{H}_y^{\,n}}{\partial t}+\dfrac{\partial\delta\vec{E}_z^{\,n}}{\partial x}\end{bmatrix}d\Gamma dt + \sum_{n=1}^{N}\int_0^T\int_\Gamma\vec{e}_z^{\,n}\left(\frac{\partial\delta\vec{H}_y^{\,n}}{\partial x}-\frac{\partial\delta\vec{H}_x^{\,n}}{\partial y}-\varepsilon\frac{\partial\delta\vec{E}_z^{\,n}}{\partial t}-\sigma\delta\vec{E}_z^{\,n}\right)d\Gamma dt + (-\sum_{n=1}^{N}\int_0^T\int_\Gamma\delta\varepsilon\vec{e}_z^{\,n}.\frac{\partial\vec{E}_z^{\,n}}{\partial t}d\Gamma dt) \qquad (3)$$

Careful examination of the right-hand-side (RHS) terms of equation (3) reveals the following important points. First, the first and second terms must be equal to zero resulting in the fulfillment of Maxwell equations. Solving them in the time interval [0 T] constitutes the forward problem in which the electromagnetic fields inside the domain is sought for a given permittivity distribution. Second, the third, fourth and fifth terms are related directly to the adjoint fields. Integrating these terms by parts in time and space and assembling the similar terms yields the following

$$\{T3+T4+T5)=\sum_{n=1}^{N}\int_{0}^{T}\iint_{\Gamma}\Bigg[\delta\vec{E}_z^{\,n}\Bigg(\varepsilon\frac{\partial\vec{e}_z^{\,n}}{\partial t}+\frac{\partial\vec{h}_y^{\,n}}{\partial x}-\frac{\partial\vec{h}_x^{\,n}}{\partial y}-\sigma\vec{e}_z^{\,n}$$

$$+\sum_{n=1}^{M}(\vec{E}_z^{\,n,m}-\vec{E}_z^{\,'n,m})-\Bigg)+[\,\delta\vec{H}_x^{\,n}\quad\delta\vec{H}_y^{\,n}]\begin{bmatrix}\mu\dfrac{\partial\vec{h}_x^{\,n}}{\partial t}+\dfrac{\partial\vec{e}_z^{\,n}}{\partial y}\\ \mu\dfrac{\partial\vec{h}_y^{\,n}}{\partial t}-\dfrac{\partial\vec{e}_z^{\,n}}{\partial x}\end{bmatrix}\Bigg]d\Gamma dt$$

$$+\sum_{n=1}^{M}\int_{\Gamma}\left(\mu\vec{h}_x^{\,n}\delta\vec{H}_x^{\,n}+\mu\vec{h}_y^{\,n}\delta\vec{H}_y^{\,n}-\varepsilon\vec{e}_z^{\,n}\delta\vec{E}_z^{\,n}\right)_0^T d\Gamma$$

$$+\sum_{n=1}^{N}\int_{0}^{T}\int_{x}\left(\delta\vec{E}_z^{\,n}\vec{h}_x^{\,n}-\vec{e}_z^{\,n}\delta\vec{H}_x^{\,n}\right)_0^{l_y}dxdt$$

$$+\sum_{n=1}^{N}\int_{0}^{T}\int_{x}\left(\delta\vec{E}_z^{\,n}\vec{h}_x^{\,n}-\vec{e}_z^{\,n}\delta\vec{H}_x^{\,n}\right)_0^{l_y}dxdt \qquad (4)$$

By equating equation (4) to zero, the condition necessary for the minimization of an augmented cost function is derived. In so doing, the first term on the RHS of equation (4) is equated to zero, which results-in the adjoint fields satisfying Maxwell's equations with the current source terms replaced with error signals calculated as the different between the computed and measured electric field at the measurement points. For the second term in equation (4) to be zero, the adjoint fields should be traveling back-ward in time. Moreover, the third and forth terms cancel each other when the adjoint fields follow the same boundary condition as in the forward problem. Therefore, by simply changing the variable in time, the adjoint fields can also be calculated using the FDTD approach. Finally, the sixth term on the RHS of equation (3) represents the gradient of an augmented cost function.

C. Inversion strategies

The gradient of augmented cost function with respect to the permittivity can be easily identified by examining equation (4) closely. Mathematically it is given as follows

$$\frac{\partial F^a}{\partial\varepsilon}=-\sum_{n=1}^{N}\int_{0}^{T}\iint_{\Gamma}\vec{e}_z^{\,n}\cdot\frac{\partial\vec{E}_z^{\,n}}{\partial t}d\Gamma dt \qquad (5)$$

This formula can be utilized by any gradient based optimization techniques for minimization of augmented cost function. Among them, the most commonly used techniques is the Polak–Ribiére non-linear conjugate gradient method [14]. Using this method, the updating process for the current estimate of the dielectric properties of unknown target is given by

$$\varepsilon^{k+1}=\varepsilon^{k}+\alpha^{k}v^{k} \qquad (6a)$$

where v^{k} is given by

$$v^{k}=-g^{k}+\beta^{k}v^{k-1} \qquad (6b)$$

where ε^{k+1} and ε^{k} are the current and previous estimate of permittivity, α^{k} is the step size in the direction of conjugate gradient, v^{k} and v^{k-1} are the current and previous conjugate gradient directions, g^{k} is the gradient of the augmented cost function, and β^{k} is given by

$$\beta^{k}=\frac{g^{k}\cdot g^{k}-g^{k-1}}{\left\|g^{k-1}\right\|^{2}} \qquad (6c)$$

The Newmann series solution is obtained by iteratively solving equations (5-6) until convergence is reached or when the maximum number of iteration is exceeded.

There are two major issues associated with the use of the above optimization technique. First, the problem with local minima and second is the time consuming nature of the procedures. These problems become more complicated when the search region is large compared to a wave-length. To overcome these difficulties a special case solution can be obtained by carefully examining (6). One such case is that when $k=0$ and $\alpha^{0}=1$, is the first iteration and the solution to inverse scattering becomes Born approximation. Following this and letting $k=0$ and $\alpha=1$ in equations (6), we have derived a single-step time domain inverse scattering technique and its updating equation is given by

$$\Delta\varepsilon=-g \qquad (7)$$

Meanwhile the Newman series approximation is obtained by iteratively updating the solution via the Polak-Ribiére algorithm as mentioned previously. The methods needed for calculating the gradients and adjoint fields are similar to the single-step algorithm. In this case convergence is assumed after the iteration has exceeded 20th step. Even though other systematic approach can be used to terminate the algorithm, however, a fairly good reconstructions are possible after 20th iterations as results in this paper demonstrated.

III. RESULTS AND DISCUSSION

In order to assess the fidelity and accuracy of these inversion strategies, both numerical and experimental data are performed. Two different grid sizes are used in this study. In the first one the computation domain is descritized into 22x52 cells from which 20x40 grid points constitute the imaging region. Meanwhile the second and finer grid is made-up of 210x410 cells from which 200x400 grid points constitute the imaging region. The coarser and finer grids are used to implement the iterative and single-step image reconstruction algorithm respectively. In both cases, the imaging plane is illuminated by transverse magnetic (TM) waves generated by 20 transmitters placed on one side of the scaterrer. For each transmitter position, the electric field is measured by 20 receiver placed on the opposite side. Modulated Gaussian pulse with central frequency 1GHz is assumed for both simulation and experimental results. Fig 2. shows the excitation signal, its spectrum and first derivative respectively.

A. *Simulation Results*

Two simulation examples are performed using the coarser grid in order to validate the methods and procedures above described. It is also assumed that the medium is lossy with

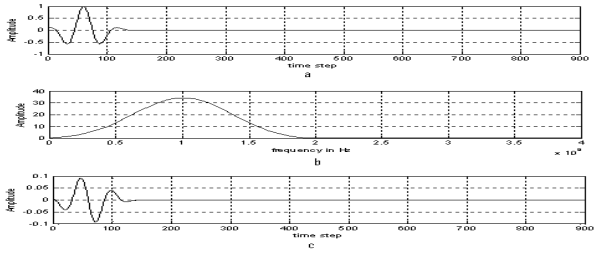

Fig. 2 Example of excitation signals assumed in the reconstruction, (a) modulated cosine Gaussian with 1 GHz central frequency, (b) its spectrum, and, (c) is the derivative of (a)

$\varepsilon_r = 30$, $\sigma = 1\,mS/m$, and μ is set equal to free space value. In the first simulation 4 cm square object ($\varepsilon_r = 35$) is placed at the center of the imaging plane while in the second example two 4x6 cm rectangular objects ($\varepsilon_r = 35$) are placed 18 cm apart. Based on the frequency of the excitation signal together with the electrical properties of the medium, the maximum possible time step, Δt, determined by the Courant stability criteria [16] is $129\,ps$. Here, $\Delta t = 32.5\,ps$ is used thus fulfilling this condition. The time interval used in the computation is fixed to 400 time steps corresponding to the imaging period of $[0,13]$ns.

The reconstruction profiles of one and two objects using the single step and iterative inversion algorithms are shown in Figs. 3-6. In Fig. 3, (a) is the actual image, (b) is the single-step reconstruction (c) is the image reconstructed using iterative technique. Fig. 4(a) and (b) correspond to images in Fig. 3(a) and (c) respectively but plotted in 2-D. Meanwhile a graph in Fig. 4(c) shows the convergence trend of the iterative algorithm. In this example the reconstruction is terminated after 16th step. The two-object reconstructions are shown in Figs.4-5. As before, Fig. 4(a) shows the actual image, 4(b) is the single-step reconstruction and 4(c) is the iterative reconstruction. The 2-D representations of these images are shown in Fig. 6(a) and (b), while Fig. 6(c) displays the convergence trend of the iterative scheme. In the of iterative scheme the algorithm is terminated after 21st step. Clearly, it can be seen from Figs. 3 and 5 that both algorithms can accurately estimate the shape, size and location of unknown scatterer. As expected the iterative technique resulted in a more accurate reconstruction compared to a single-step technique. However, in both cases, the reconstruction shows some error asymmetrically along the horizontal direction since the measurements are performed in lateral view only. The same trend is also observed in Fig.4. The sizes and locations of the objects are correctly reconstructed even though their shapes and sizes appear distorted in x-direction. However, the distortion is less when the iterative technique is employed. Although the iterative technique is more superior compared to the single-step algorithm, the latter is much faster and the convergence is always assured. Implemented on 2.5 GHz Intel quad-core processor with 2GByte of memory, the single-step takes slightly less than 60 seconds compared to more than 13 hours for the iterative technique. If speed is crucial factor, then it can be shown here that a single-step reconstruction algorithm with an adequate smoothing filter offers an alternative solution especially when reconstruction is attempted on large scale 2-D or 3-D problems.

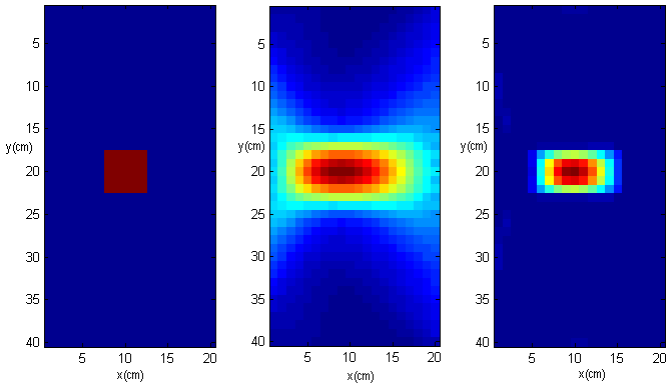

Fig. 3 Simulation results for one object at center, (a) actual image, (b) reconstructed image using single step, and, (c) reconstructed image using iterative algorithm

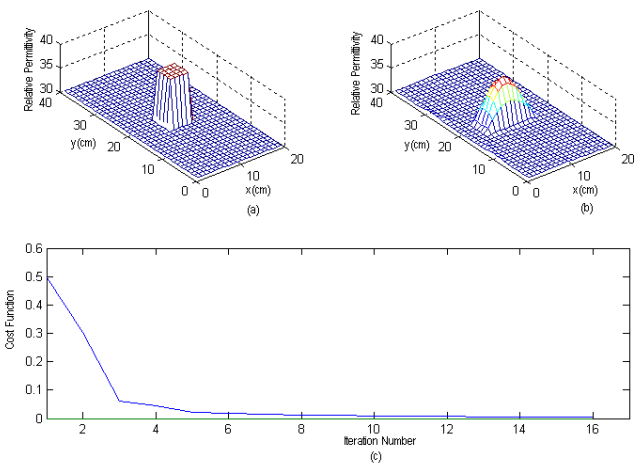

Fig. 4 A 3-D representation of Fig. 3, (a) actual profile. (b) reconstructed profile after 16 iterations, and, (c) the convergence trend

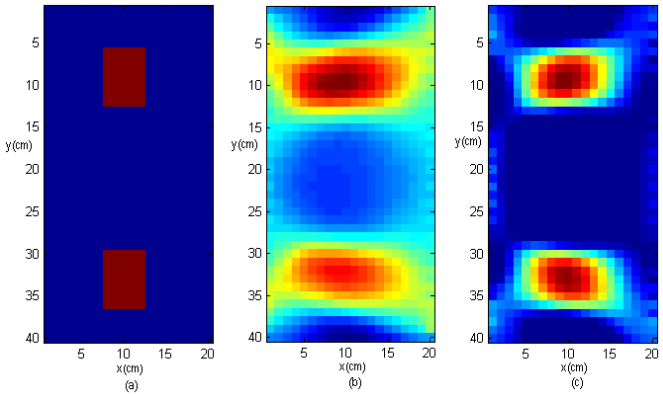

Fig. 5 Simulation result for two objects, (a) actual image (b) reconstructed image using single step, and (c) reconstructed image using iterative algorithm

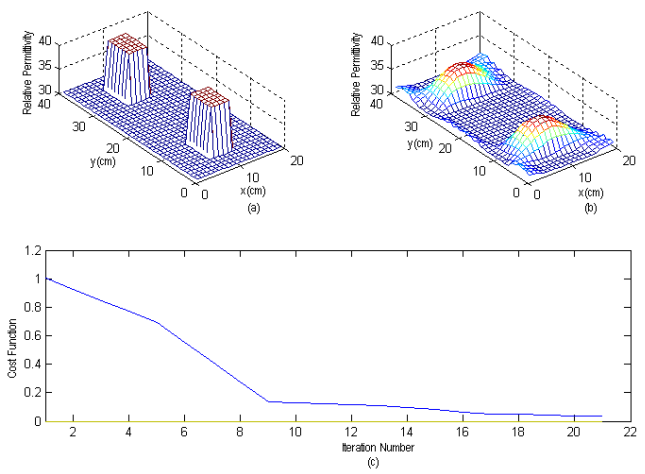

Fig. 6 A 3-D representation of Fig. 5, (a) actual profile, (b) reconstructed profile after 16 iterations, and (c) the convergence trend

B. Experimental Results

The reliability of the single-step reconstruction algorithm is further assessed using two experiments and following the same geometry described elsewhere [9]. In the first experiments, one biological target in the form of ellipsoids-shape pumpkin with fattest and thinnest diameter with 9 and 5cm respectively is placed at the centre of the imaging plane while in the second experiment, two plastic rods with different size and shape are placed at two different locations. The first one is a cylindrical pipe with 2.5 cm diameter located at the upper half of imaging plane while the second is the 5x6 cm rectangular object placed slightly below the centre. The first experiment is performed using antenna with centre frequency of 1 GHz while the second one is accomplished using 0,9 GHz antenna. Altogether 400 unique measurements are recorded for each experiment. Each measurement represents transmitter–receiver pair, containing 801 samples each for real and imaginary components. The scanning times are fixed to 8.5 ns and 13.ns for the first and second experiments respectively. The difference in time is due to the different in centre frequency of the antenna.

The cornerstone of our inversion algorithm is the gradient which is already known to be zero for same homogenous medium. However, this is not the case due to the experimental and modeling errors. Therefore, calibration is performed to minimize these errors. This ensures that the gradient calculated from known distribution agreed with gradient obtained by simulation. The calibration strategy is adopted in order to ensure that the measured signals and calculated signals from the model are in close agreement for a defined set-up. The aim of this procedure is to minimize systematic errors between the experimental system and the model, such as antenna gains, positioning errors, cable propagation delays and such like. The procedure involves comparing the measured and simulated signals for the case of a fixed homogeneous medium. The measured values are then time-shifted to coincide with the simulated data and their amplitudes normalized. Following this time alignment and normalization, the remaining residual errors are calculated by simply subtracting the calculated and measured signals. This resultes in a residual error matrix of size $m \times n$ with $m = T - 1$ and $n = NM$. Subsequent measurements are then corrected by applying the appropriate time offset, gain correction values, and subtraction of their residual errors. Fig. 7 shows the pulse obtained from one projection before and after calibration. From this figure it can be seen that the measured signal approximately matches the simulated one after calibration. Indirectly, this procedure minimized errors inherent in the FDTD modeling and ensures that these errors are not carried on into the image reconstruction procedure.

All data measured are treated in the same way prior to reconstruction. Fig. 8 and Fig. 9 show the image reconstruction obtained from first and second experiments respectively. Referring to these figures, (a) are actual images (b) are images reconstructed using Born series approximation and (c) are corresponding images in (b) after smoothing. Clearly, it can be seen from this figure that the algorithm can accurately detect and localize the biological target despite low signal to noise ratio, although its size appears exaggerated due to the approximation in the algorithm. Furthermore, the detailed features within the target are absent from the tomogram. This must be expected since the size and variation of such features are electrically small compared to wavelength used. The results from plastic rods experiment are shown in Fig.7. Again, it can be seen here that the location, shape, and size of objects are accurately reconstructed; however there are some artifacts in shape reconstruction particularly the rectangular rod in which the four edges appeared smooth. This is due to the effect of processing this image using a low-pass filter.

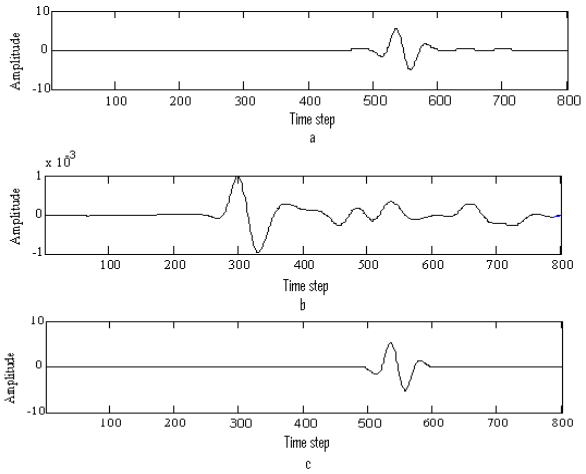

Fig. 7 Calibration of the imaging instrument showing the waveform pattern obtained from one projection, (a) the simulated pulse, (b) the measured pulse and (c) the calibrated pulse

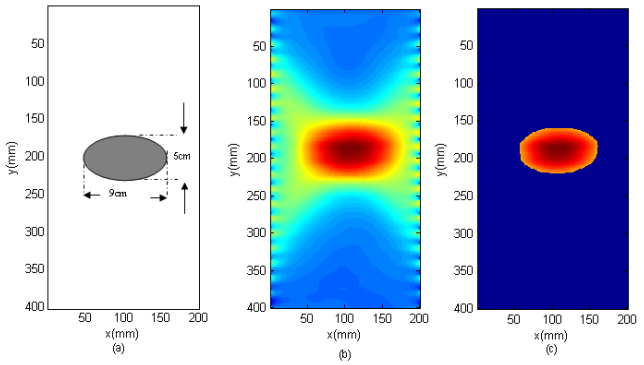

Fig. 8 Image reconstruction of a pumpkin located at the center, (a) actual, (b) reconstructed before smoothing, and (c) reconstructed after smoothing

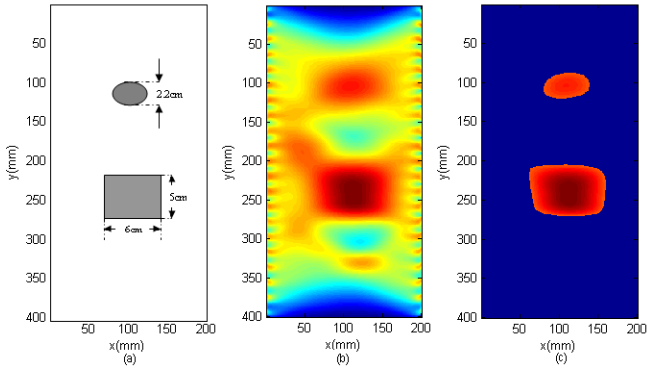

Fig. 9 Image reconstruction of two plastic phantoms of different sizes and shapes, (a) actual, (b) reconstructed before smoothing, and (c) reconstructed after smoothing

IV. CONCLUSIONS

Two inversion time domain inverse scattering schemes, which combine the FDTD and gradient based minimization scheme has been discussed and implemented. The gradient has formerly been computed using Fréchet derivative and adjoint method. The first algorithm has been based on Born approximation, permitting the image reconstruction be performed in single-step. In contrast, the second algorithm utilized the iterative Polak–Ribiére method, leading to a Newman series solution. The practical feasibility of these algorithms has been investigated by using simulated experiments and real data. In the first experiment, a biological object was added to simulate cancerous-like dielectric profile, while the second experiment used plastic for performance and testing purposes. It has been discovered that the Newman solutions are more accurate compared to Born series approximation although the former technique takes much longer time to converge. It has also been shown here that the quality of images produced by Born approximation can further be improved by filtering. Therefore, a compromise between speed and accuracy can be achieved via a single-step technique provided a suitable filter can be designed for image enhancement.

ACKNOWLOEDGEMENT

The authors acknowledge support from USM for funding this project under the Research University grant scheme (1001.PELECT.814012).

REFERENCES

[1] Lazebnik, M., et al.,*A large-scale study of the ultrawideband microwave dielectric properties of normal, benign and malignant breast tissues obtained from cancer surgeries.* Phys. Med. Biol. **52** (2007) 6093–6115

[2] Franchois, A. and C. Pichot, *Microwave imaging-complex permittivity reconstruction with a Levenberg-Marquardt method.* Antennas and Propagation, IEEE Transactions on, 1997. **45**(2): p. 203-215.

[3] Caorsi, S., G.L. Gragnani, and M. Pastorino, *Two-dimensional microwave imaging by a numerical inverse scattering solution.* Microwave Theory and Techniques, IEEE Transactions on, 1990. **38**(8): p. 981-980.

[4] Rekanos, I.T. and T.D. Tsiboukis, *A combined finite element-nonlinear conjugate gradient spatial method for the reconstruction of unknown scatterer profiles.* Magnetics, IEEE Transactions on, 1998. **34**(5): p. 2829-2832.

[5] Tijhuis, A., *Iterative determination of permittivity and conductivity profiles of a dielectric slab in the time domain.* Antennas and Propagation, IEEE Transactions on, 1981. **29**(2): p. 239-245.

[6] Weedon, W.H. and W.C. Chew *Time domain inverse scattering using the local shape function (LSF) method* Inv. problems 1993. **9**: p. 551-564.

[7] Chung, Y., -S., C. Cheon, and S. Hahn, -Y.,, *Reconstruction of dielectric cylinders using FDTD and topology optimization technique.* Magnetics, IEEE Transactions on, 2000. **36**(4): p. 956-959.

[8] Zhou, H., T. Takenaka, and T. Tanaka. *3D reconstruction of a lossy object using time-domain data transmitted and received with dipole antennas*. in *Antennas and Propagation Society International Symposium, 2003. IEEE*. 2003.

[9] Abenius, A. and B. Strand, *Solving inverse electromagnetic problems using FDTD and gradient-based minimization.* Int. J. Numer. Methods Eng. , 2006. **68**: p. 650-673.

[10] Xie, C.G., et al., *Electrical capacitance tomography for flow imaging-system model for development of image reconstruction algorithms and design of primary sensors.* IEE Proceedings-G

. **139**(89): p. 89-98.

[11] Abdullah, M.Z., et al., *Ultra wide band imaging of dielectric in the time domain using sensitivity coefficient based reconstruction* in *5th world congress industrial on industrial process tomography* 2007: Bregen , Norway

[12] Abdullah, M.Z., et al., *Time domain reconstruction using sensitivity coefficients for limited view ultra wide band tomography* Rev. Sci. Instrum. , 2007. **78**(1): p. 1-10.

[13] Rekanos, I.T. and A. Raisanen, *Microwave imaging in the time domain of buried multiple scatterers by using an FDTD-based optimization technique.* Magnetics, IEEE Transactions on, 2003. **39**(3): p. 1381-1384.

[14] Luenberger, D.G., *Linear and Non linear programing* 1984: Reading MA Addison-Wesly

[15] Mur, G., *Absorbing Boundary Conditions for the Finite-Difference Approximation of the Time-Domain Electromagnetic-Field Equations.* Electromagnetic Compatibility, IEEE Transactions on, 1981. **EMC-23**(4): p. 377-382.

[16] Kunz, K., S. and R. Luebbers, J., *The Finite Difference Time Domain Method for Electromagnetics*. 1993: CRC-Press. 636 g.